

Clustering of Local Extrema in *Planck* CMB maps

A. Vafaei Sadr¹ & S. M. S. Movahed^{2,3*}

¹ School of Physics, Institute for Research in Fundamental Sciences (IPM), P. O. Box 19395-5531, Tehran, Iran

² Department of Physics, Shahid Beheshti University, Velenjak, P. O. Box 1983969411, Tehran, Iran

³ Ibn-Sina Multidisciplinary Laboratory, Department of Physics, Shahid Beheshti University, Velenjak, P. O. Box 1983969411, Tehran, Iran

3 March 2022

ABSTRACT

The clustering of local extrema including peaks and troughs will be exploited to assess Gaussianity, asymmetry and the footprint of cosmic strings network on the CMB random field observed by *Planck* satellite. The number density of local extrema reveals some non-resolved shot noise in *Planck* maps. The SEVEM data has maximum number density of peaks, n_{pk} , and troughs, n_{tr} , compared to other observed maps. The cumulative of n_{pk} and n_{tr} above and below a threshold, ϑ , for all *Planck* maps except for the 100GHz band are compatible with the Gaussian random field. The unweighted Two-Point Correlation Function (TPCF), $\Psi(\theta; \vartheta)$, of the local extrema illustrates significant non-Gaussianity for angular separation $\theta \leq 15'$ for all available thresholds. Our results show that to put the feasible constraint on the amplitude of the mass function based on the value of Ψ around the *Doppler peak* ($\theta \approx 70' - 75'$), we should consider $\vartheta \gtrsim +1.0$. The scale independent bias factors for peak above a threshold for large separation angle and high threshold level are in agreement with that of expected for a pure Gaussian CMB. Unweighted TPCF of local extrema demonstrates a level of rejecting Gaussian hypothesis in SMICA. Genus topology also confirms the Gaussian hypothesis for different component separation maps. Tessellating CMB map with disk of size 6° based on n_{pk} and Ψ_{pk-pk} demonstrate statistical symmetry in *Planck* maps. Combining all maps and applying the Ψ_{pk-pk} puts the upper bound on the cosmic string's tension: $G\mu^{(up)} \lesssim 5.00 \times 10^{-7}$.

Key words: methods: data analysis - methods: numerical - methods: statistical - cosmic microwave background ; theory - early Universe.

1 INTRODUCTION

Cosmological stochastic fields are ubiquitous in various observations. Any conceivable theory incorporating initial conditions (Malik & Wands 2009), cosmic microwave background (CMB) (Dodelson 2003; Lesgourgues et al. 2013; Lesgourgues 2013; Ade et al. 2016b), large scale structures (Bernardeau et al. 2002; Cooray & Sheth 2002) and other relevant fields (Kashlinsky 2005; Lewis & Challinor 2006) essentially includes stochastic notion. The initial conditions and/or evolution for cosmological fields are specified with random behavior. To infer any reliable bridge between model building and observational quantities, it is necessary to use robust statistical tools. By means of Central Limit Theorem and statistical isotropy, it is possible to use a perturbative approach to characterize stochastic field (Matsubara 2003; Codis et al. 2013; Matsubara 2020).

Many topological and geometrical measures have been introduced to characterize morphology of cosmological stochastic fields, \mathcal{F} , in $1+1$, $1+2$ and $1+3$ dimensions¹. Critical and excursion sets are generally the backbone for the definition of more significant features on smoothed stochastic field. Critical sets include features incorporating conditions for having local and extended extrema (Matsubara 2003; Pogosyan et al. 2009; Gay et al. 2012; Codis et al. 2013; Matsubara 2020). A rigorous definition for excursion sets for a function of given stochastic field, $\mathcal{F}(X)$, above a

¹ According to the *measure theoretic* approach which is ultimately identical to a probabilistic description, a typical $(n+D)$ -Dimensional stochastic field, $\mathcal{F}^{(n,D)}$, is a measurable mapping from probability space into a σ -algebra of \mathbb{R}^n -valued function on \mathbb{R}^D Euclidian space (Adler 1981; Adler & Taylor 2011; Adler et al. 2010). We suppose that the index n refers to n -dependent parameters and D represents D -independent parameters describing a $(n+D)$ -Dimensional random field or a stochastic process.

* E-mail: m.s.movahed@ipm.ir

threshold ϑ is defined by: $\mathcal{A}_\vartheta(\mathcal{F}) \equiv \{X|\mathcal{F}(X) \geq \vartheta\}$ (Adler 1981). Accordingly, in real or harmonic spaces, we are able to achieve theoretical descriptions for the corresponding features in a cosmological stochastic field irrespective of its dimension. The mentioned benchmarks have advantages and disadvantages from theoretical and computational points of view. Complicated algorithms and marginal behavior with respect to an arbitrary exotic feature are some of the disadvantages. Nevertheless, there are many benefits to set up such estimators beyond standard methods. Among them are the magnification of deviation and capability to discriminate the exotic features embedded in a typical cosmological field.

One-point statistics provides significant information regarding the abundance of the underlying features while the complex nature of cosmological stochastic fields is essentially going beyond one-point analysis. To characterize such complexity, we should take into account much more complicated behavior in precise observations. Subsequently, N -point correlation functions of arbitrary features are therefore common estimators. In the context of Two-Point Correlation Function (TPCF), there are two relevant measures to assess clustering: I) weighted TPCF deals with the autocorrelation and II) unweighted TPCF estimates the excess probability of finding a pair of features by imposing a typical condition for a given distance (or e.g. time, angle) separation (Peebles 1980; Kaiser 1984; Peacock & Heavens 1985; Lumsden et al. 1989; Bardeen et al. 1986; Bond & Efstathiou 1987; Davis & Peebles 1983; Hamilton 1993; Szapudi & Szalay 1998; Hewett 1982; Landy & Szalay 1993a). In principle, there is a systematic relation between both TPCFs (Rice 1954; Taqqu 1977; Kaiser 1984; Szalay 1988a; Desjacques et al. 2010, 2018).

Level crossing statistics is a pioneered approach for characterizing stochastic processes introduced by S. O. Rice (Rice 1944, 1945). Up-, down- and conditional crossing statistics are modifications to primary definition of level crossing (Bardeen et al. 1986; Bond & Efstathiou 1987; Ryden 1988; Ryden et al. 1989; Matsubara 1996; Brill 2000; Matsubara 2003; Shahbazi et al. 2003; Movahed & Khosravi 2011; Ghasemi Nezhadhighi et al. 2017). Minkowski functionals which are also closely related to the crossing statistics are capable to provide $(1+D)$ functionals to quantify morphology in D -dimension (über Inhalt 1957) and have been utilized for cosmological random fields (Mecke et al. 1994; Schmalzing et al. 1995; Schmalzing & Górski 1998; Matsubara 2003, 2010; Hikage et al. 2006; Codis et al. 2013; Ling et al. 2015; Fang et al. 2017). A number of critical sets including peaks (hills), troughs (lakes), saddles, voids, skeleton, genus and Euler characteristics, are more popular in cosmology for different purposes and they have been fully explored for Gaussian stochastic fields. Some extensions for non-Gaussian and anisotropic conditions have been done in some researches (Matsubara 2003; Pogosyan et al. 2009, 2011; Gay et al. 2012; Codis et al. 2013). More recently, Betti numbers, Euler characteristic and Minkowski functionals for a set of cosmological $3D$ fields have been examined extensively (Pranav et al. 2019). The scaling approach for investigation cosmological stochastic fields has been discussed by Borgani (1995); Movahed et al. (2011). Standard estimators like three- and four-point functions in real space, bispectrum and trispectrum in harmonic space, multiscaling methods such as wavelet (Lewis et al. 2016; Ade et al. 2014c, and ref-

erences therein) and regenerating of stochastic process based on Fokker-Planck equation (Ghasemi et al. 2006) have been also considered.

CMB has stochastic nature encoded by various phenomena ranging from high energy and primordial events to low energy scales (Dodelson 2003; Lesgourgues et al. 2013; Lesgourgues 2013; Ade et al. 2016b). Some of more relevant topics for examining the CMB by statistical tools are as follows: different anomalies (Ade et al. 2016c), non-Gaussianity (Ade et al. 2014c; Lewis et al. 2016; Renaux-Petel 2015) and other exotic phenomena (Ade et al. 2014d; Vafaei Sadr et al. 2018, 2017; Movahed et al. 2013; Movahed & Khosravi 2011).

Peaks and pixels statistics are proper measures of CMB in one- and two-point forms and have been extensively carried out to assess CMB data released by various surveys (Sazhin 1985; Bond & Efstathiou 1987; Vittorio & Juszkiewicz 1987; Cayon & Smoot 1995; Fabbri & Torres 1996; Kogut et al. 1995, 1996; Barreiro et al. 1997; Heavens & Sheth 1999; Heavens & Gupta 2001; Kashlinsky et al. 2001; Futamase & Takada 2000; Doré et al. 2003; Hernández-Monteagudo et al. 2004; Hou et al. 2009; Tojeiro et al. 2006; Larson & Wandelt 2004, 2005; Rossi et al. 2009, 2011; Pogosyan et al. 2011; Movahed et al. 2013; Rossi 2013; Vafaei Sadr et al. 2018, 2017). $2D$ genus topology which is related to the statistics of hot and cold spots of the underlying field has been evaluated for CMB random field (Colley & Richard Gott III 2003; Gott et al. 2007; Colley & Gott III 2015). Persistent homology in the context of Topological Data Analysis has been considered for searching the non-Gaussianity in the CMB map (Cole & Shiu 2018). Also the detectability of gravitational lensing in the CMB map based on the TPCF of hot spots has been examined by Takada et al. (2000); Takada & Futamase (2001). Assessment of various researches indicates that clustering evaluation in CMB maps for different purposes has been almost concentrated on statistics of regions above or below a threshold without taking into account proper conditions on the first and second derivatives properties of underlying field (Kashlinsky et al. 2001; Rossi et al. 2009, 2011; Rossi 2013). In this paper, however we will focus on the clustering of local extrema to examine whether such critical sets are more sensitive to declare exotic features embedded in CMB map as well as their robustness in the presence of noise.

Here, we deal with the local extrema statistics of the *Planck* CMB maps to study the following main objects and novelties:

- 1) Assessment of noise, point-like sources and other contaminations for different bands and map extraction pipelines. Accordingly, we will be able to examine the internal consistency and robustness of different component separation algorithms based on clustering of peaks and troughs. Since the beam transfer function used for map extraction is different for each pipelines, we expect that the TPCF of peaks associated with various components is more sensitive to the contribution of foreground and point-like sources in different manners. Subsequently, cross-correlation of unweighted pixels incorporating conditions for having extrema enables us to control and to increase the performance and robustness of CMB map for cosmological implementations.
- 2) We will also probe the non-Gaussianity based on capability of local extrema clusterings.
- 3) The scale dependent and independent bias factors accord-

ing to its general definition will be determined for different components.

4) Asymmetry anomaly will be investigated by means of unweighted TPCF of peaks for various component separations and different degradations.

5) We will compute the value of upper bound on the cosmic string tension, by comparing clustering of critical sets computed for pure Gaussian CMB maps including all foregrounds, systematic noises and beam effect and those induced by cosmic strings network simulated according to numerical simulations of Nambu-Goto string networks using the Bennett-Bouchet-Ringeval code (Bennett & Bouchet 1990; Ringeval et al. 2007).

The rest of this paper is organized as follows: in section 2, mathematical description of local extrema statistics will be clarified. Genus topology and statistical definition of bias factor will be given in this section. Data description will be given in section 3. We will implement the geometrical and topological measures on the synthetic and real CMB data in section 4. Gaussian and asymmetry hypotheses and searching the cosmic strings network on CMB map in section 4. The last section will be devoted to summary and conclusions.

2 THEORETICAL NOTIONS

The statistics of local extrema (both minima and maxima) provides a robust framework to search for evidence of non-Gaussianity in the data (Matsubara 2003; Tojeiro et al. 2006; Pogosyan et al. 2009, 2011; Matsubara 2020) and to look for exotic features such as topological defects (e.g. cosmic strings network) (Heavens & Sheth 1999; Heavens & Gupta 2001; Movahed et al. 2013; Vafaei Sadr et al. 2017, 2018). Such an extremum is defined as a pixel whose amplitude is higher or lower than the adjacent nearest neighbors incorporating conditions on first and second derivatives of field. Therefore, we have additional mathematical conditions when we deal with extrema compared to sharp clipping on a typical stochastic field.

For a statistically isotropic Gaussian stochastic field, number density of peaks was derived by Bond & Efstathiou (1987). The non-Gaussian extrema counts for the CMB field have been studied by Pogosyan et al. (2011). It has been expressed that according to the perturbation approach for smooth non-Gaussian field, it is possible to track different shapes of non-Gaussianity (Pogosyan et al. 2011). However, Movahed et al. (2013) showed that the footprint of non-Gaussianity produced by cosmic strings network can not be recognized by utilizing only number count of extrema. Subsequently, we conclude that clustering of coldspots and hotspots manifested by extrema outliers in the trough and peak values can constitute evidence for non-Gaussianity or deviation from isotropy (Ade et al. 2016c).

2.1 Local extrema counts and excursion sets

For the sake of clearance, we will specify number density of local extrema, number density of regions above (below) a threshold and unweighted two-point correlation function of critical sets in the probabilistic framework for CMB map.

[t]

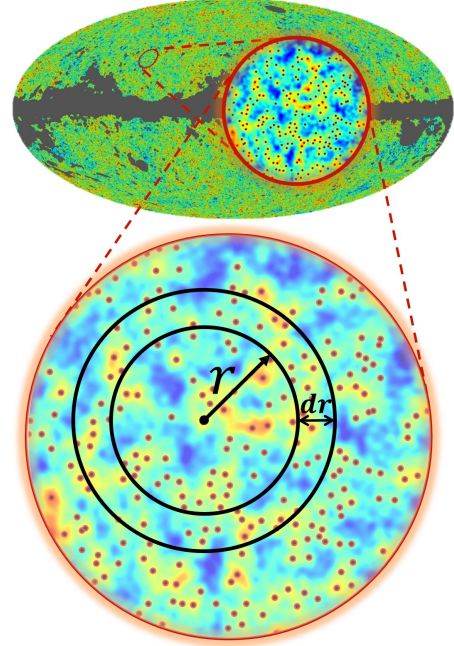


Figure 1. Peaks distribution on the NILC map for $N_{\text{side}} = 512$ at threshold $\vartheta = 0.5$. In the zoom-in plot, we indicate a sketch to illustrate clustering of local peaks separated by r .

The CMB temperature anisotropy is a stochastic field, represented by a 2D map, $T \in L^2(\mathbb{R}^2)$, either observed or simulated. We define the vector \mathcal{A} at each spatial point represented by (θ, ϕ) on the CMB map by:

$$\mathcal{A}_\mu \equiv \{\delta_T, \eta_\phi, \eta_\theta, \xi_{\phi\phi}, \xi_{\theta\theta}, \xi_{\phi\theta}\}$$

where $\delta_T \equiv \Delta T(\theta, \phi)/T(\theta, \phi)$ is the temperature fluctuation, $\eta_\phi \equiv \partial\delta_T/\partial\phi$, $\eta_\theta \equiv \partial\delta_T/\partial\theta$ and $\xi_{\phi\theta} \equiv \partial^2\delta_T/\partial\phi\partial\theta$. For examining local extrema, we therefore need the first and second order derivatives. To determine the joint probability density function (PDF) of \mathcal{A} , we use the so-called characteristic function defined by:

$$\mathcal{Z}_\mathcal{A}(\lambda) = \int_{-\infty}^{+\infty} d^6\mathcal{A} \mathcal{P}(\mathcal{A}) e^{i\lambda \cdot \mathcal{A}} \quad (1)$$

where λ is an array with the same size as \mathcal{A} . The perturbative expansion of \mathcal{Z} becomes (Matsubara 2003):

$$\begin{aligned} \mathcal{Z}_\mathcal{A}(\lambda) = & \exp\left(-\frac{1}{2}\lambda^T \mathcal{K}^{(2)} \lambda\right) \\ & \times \exp\left[\sum_{j=3}^{\infty} \frac{i^j}{j!} \left(\sum_{\mu_1}^N \sum_{\mu_2}^N \dots \sum_{\mu_j}^N \mathcal{K}_{\mu_1, \mu_2, \dots, \mu_j}^{(j)} \lambda_{\mu_1} \lambda_{\mu_2} \dots \lambda_{\mu_j}\right)\right] \end{aligned} \quad (2)$$

where $\mathcal{K}_{\mu_1, \mu_2, \dots, \mu_n}^{(n)} \equiv \langle \mathcal{A}_{\mu_1} \mathcal{A}_{\mu_2} \dots \mathcal{A}_{\mu_n} \rangle$ is the array of connected cumulants. Also $\mathcal{K}^{(2)} \equiv \langle \mathcal{A} \otimes \mathcal{A} \rangle$ represents the 6×6 covariance matrix of \mathcal{A} at each spatial point. In the appendix, we give a details for the elements of covariance matrix.

The joint probability density function of CMB map incorporating higher order derivatives of δ_T can be inferred by the inverse Fourier transform of the characteristic function

(Eq. (2)) as:

$$\mathcal{P}(\mathcal{A}) = \exp \left[\sum_{j=3}^{\infty} \frac{(-1)^j}{j!} \left(\sum_{\mu_1=1}^6 \dots \sum_{\mu_j=1}^6 \mathcal{K}_{\mu_1, \mu_2, \dots, \mu_j}^{(j)} \times \frac{\partial^j}{\partial \mathcal{A}_{\mu_1} \dots \partial \mathcal{A}_{\mu_j}} \right) \right] \mathcal{P}_G(\mathcal{A}) \quad (3)$$

where $\mathcal{P}_G(\mathcal{A}) = \frac{1}{\sqrt{(2\pi)^6 |\mathcal{K}^{(2)}|}} e^{-\frac{1}{2}(\mathcal{A}^T \cdot [\mathcal{K}^{(2)}]^{-1} \cdot \mathcal{A})}$. The perturbative form of the one-point PDF of the temperature fluctuations, $\mathcal{P}_{\delta_T}(\alpha)$, in the presence of weak non-Gaussianity has been derived in (Vafaei Sadr et al. 2017).

Theoretical definition of local extrema number density at a given threshold, $\delta_T \equiv \alpha = \vartheta \sigma_0$, is (Bardeen et al. 1986):

$$\begin{aligned} n_{\circ}(\vartheta) &\equiv \langle n_{\circ}(\vartheta; \mathbf{r}) \rangle = \langle \delta_D(\mathbf{r} - \mathbf{r}_{\circ}) \rangle \\ &= \int d^6 \mathcal{A} \delta_D(\mathbf{r} - \mathbf{r}_{\circ}) \mathcal{P}(\mathcal{A}_{\mu}) \end{aligned} \quad (4)$$

here \diamond can be replaced by "pk" for peak, "tr" for trough and "pix" for sharp clipping. The \mathbf{r}_{\circ} represents the location vector of local extrema and sharp clipping on the CMB map at threshold ϑ . The δ_D is Dirac delta function. Clarifying the relation between Dirac delta function and $d^6 \mathcal{A}$ enables us to write the mean value of local extrema density as:

$$n_{\circ}(\vartheta) = \langle \delta_D(\delta_T - \vartheta \sigma_0) \delta_D(\eta_{\phi}) \delta_D(\eta_{\theta}) |\det(\xi)| \rangle \quad (5)$$

The second derivative tensor of the CMB field (ξ_{ij}) should be *negative definite* (*positive definite*) at peak (trough) position. Finally, the number density of peaks for a purely isotropic Gaussian CMB field in the range of $[\vartheta, \vartheta + d\vartheta]$ becomes (Bardeen et al. 1986; Bond & Efstathiou 1987):

$$n_{pk}(\vartheta) = \frac{N_{pix}^{tot} e^{-\vartheta^2/2} \mathcal{G}(\Gamma, \Gamma\vartheta)}{4\pi (2\pi)^{3/2} \gamma^2} \quad (6)$$

where

$$\begin{aligned} \mathcal{G}(\Gamma, \Gamma\vartheta) &\equiv (\Gamma^2 \vartheta^2 - \Gamma^2) \left\{ 1 - \frac{1}{2} \operatorname{erfc} \left[\frac{\Gamma\vartheta}{\sqrt{2(1-\Gamma^2)}} \right] \right\} \\ &+ \Gamma\vartheta(1-\Gamma^2) \frac{e^{-\frac{\Gamma^2 \vartheta^2}{2(1-\Gamma^2)}}}{\sqrt{2\pi(1-\Gamma^2)}} \\ &+ \frac{e^{-\frac{\Gamma^2 \vartheta^2}{3-2\Gamma^2}}}{\sqrt{3-2\Gamma^2}} \left\{ 1 - \frac{1}{2} \operatorname{erfc} \left[\frac{\Gamma\vartheta}{\sqrt{2(1-\Gamma^2)(3-2\Gamma^2)}} \right] \right\} \end{aligned} \quad (7)$$

in which $\operatorname{erfc}(\cdot)$ stands for the complementary error function. The parameters Γ and γ in Eqs. (6) and (7) are defined by: $\Gamma \equiv \frac{\sigma_1^2}{\sigma_0 \sigma_2}$ and $\gamma \equiv \sqrt{2} \frac{\sigma_1}{\sigma_2}$ (Bond & Efstathiou 1987). $\Gamma \in [0, 1]$ clarifies the shape of power spectrum, while γ indicates the characteristic radius of local extrema. Also $N_{pix}^{tot} = 12N_{side}^2$ represents the total number of pixel in a given map with resolution specified by N_{side} computed by HEALPix software (Gorski et al. 2005). The various orders of spectral indices are given by:

$$\sigma_m^2 = \sum_{\ell} \frac{(2\ell+1)}{4\pi} [\ell(\ell+1)]^m C_{\ell}^{TT} W_{\ell}^2 \quad (8)$$

here W_{ℓ} is beam function and C_{ℓ}^{TT} is temperature power

spectrum. For the sharp clipping above (below) a threshold corresponding to the pixels above (below) a threshold, there are no constraints on the first and second derivative of the underlying field and therefore we have $n_{pix}(\vartheta) = \langle \Theta(\delta_T \mp \vartheta \sigma_0) \rangle$ (Θ is step function). The minus (plus) sign is for above (below) threshold. According to Eq. (3), the perturbative number density of pixels above a threshold in the non-Gaussian field (NG) reads as:

$$\begin{aligned} n_{pix}^{NG}(\alpha > \vartheta \sigma_0) &\equiv \langle \Theta(\delta_T - \vartheta \sigma_0) \rangle = \frac{N_{pix}^{tot}}{4\pi} \frac{1}{2} \operatorname{erfc} \left(\frac{\vartheta}{\sqrt{2}} \right) \\ &+ \frac{N_{pix}^{tot}}{4\pi} \left[\frac{e^{-\frac{\vartheta^2}{2}} (\vartheta^2 - 1) S_0}{6\sqrt{2\pi}} \right] \sigma_0 \\ &+ \frac{N_{pix}^{tot} e^{-\frac{\vartheta^2}{2}}}{4\pi} \left[\frac{3K_0 \vartheta (\vartheta^2 - 3) + S_0^2 \vartheta (\vartheta^4 - 10\vartheta^2 + 15)}{72\sqrt{2\pi}} \right] \sigma_0^2 \\ &+ \mathcal{O}(\sigma_0^3) \end{aligned} \quad (9)$$

where $S_0 \equiv \mathcal{K}_{111}^{(3)}/\sigma_0^4$ and $K_0 \equiv \mathcal{K}_{1111}^{(4)}/\sigma_0^6$. Eq. (9) represents a generalized form compared to the one given by (Rossi et al. 2011). Taking into account sharp clipping statistics up to $\mathcal{O}(\sigma_0)$ results in marginal behavior with respect to non-Gaussianity for $\vartheta = \pm 1$. Incorporating the various spectral indices, σ_m , yields more complicated theoretical formula for n_{pk} and n_{tr} , yielding more sensitivity to non-Gaussianity. Perturbative expansion in the weakly non-Gaussian regime for number density of peaks and troughs have been calculated in (Pogosyan et al. 2011). In Fig. 1 we show the spatial distribution of peaks on the NILC map. In the next subsection we will try to setup the clustering of local extrema which is systematically given by unweighted TPCF of peaks and troughs.

2.2 Unweighted Two-Point Correlation Function

The one-point statistics of some geometrical measures (number density of local extrema as well as pixels above a threshold) have been explained in previous subsection. They can explore probable exotic features and various types of non-Gaussianity (Pogosyan et al. 2011; Rossi et al. 2011; Rossi 2013; Gay et al. 2012; Codis et al. 2013; Reischke et al. 2015). However, to do more precise evaluation, we should go beyond one-point statistics (Hou et al. 2009; Movahed et al. 2013). In this subsection, we focus on the clustering of local extrema which is the so-called unweighted TPCF. Semi-analytical (Heavens & Sheth 1999; Heavens & Gupta 2001; Matsubara 2020) and numerical approaches (Kerscher et al. 2000) are often used to study the clustering of local extrema. The clustering of peak or trough pairs separated by distance $r = |\mathbf{r}_1 - \mathbf{r}_2|$ at thresholds ϑ_1 and ϑ_2 is given by:

$$\langle n_{\circ}(\mathbf{r}_1, \vartheta_1) n_{\circ}(\mathbf{r}_2, \vartheta_2) \rangle = \int d^6 \mathcal{A}_1 d^6 \mathcal{A}_2 \delta_D(\mathbf{r}_1 - \mathbf{r}_{\circ 1}) \delta_D(\mathbf{r}_2 - \mathbf{r}_{\circ 2}) \mathcal{P}(\mathcal{A}_1; \mathcal{A}_2) \quad (10)$$

The excess probability of finding pairs using Eq. (10) becomes:

$$\Psi_{\circ-\circ}(r; \vartheta_1, \vartheta_2) = \frac{\langle n_{\circ}(\mathbf{r}_1, \vartheta_1) n_{\circ}(\mathbf{r}_2, \vartheta_2) \rangle}{n_{\circ}(\vartheta_1) n_{\circ}(\vartheta_2)} - 1, \quad (11)$$

In our pipeline, we rely on the numerical evaluation of unweighted TPCF of local extrema in both ob-

$$\Psi_{\diamond-\diamond}^N(r; \vartheta_1, \vartheta_2) = \left(\frac{D_{\diamond}(\mathbf{r}_1, \vartheta_1) D_{\diamond}(\mathbf{r}_2, \vartheta_2)}{R_{\diamond}(\mathbf{r}_1, \vartheta_1) R_{\diamond}(\mathbf{r}_2, \vartheta_2)} \right) \frac{N_R^{\diamond}(N_R^{\diamond} - 1)}{N_D^{\diamond}(N_D^{\diamond} - 1)} - 1 \quad (12)$$

$$\Psi_{\diamond-\diamond}^H(r; \vartheta_1, \vartheta_2) = \frac{R_{\diamond}(\mathbf{r}_1, \vartheta_1) R_{\diamond}(\mathbf{r}_2, \vartheta_2) D_{\diamond}(\mathbf{r}_1, \vartheta_1) D_{\diamond}(\mathbf{r}_2, \vartheta_2)}{[D_{\diamond}(\mathbf{r}_1, \vartheta_1) R_{\diamond}(\mathbf{r}_2, \vartheta_2)]^2} - 1 \quad (13)$$

$$\Psi_{\diamond-\diamond}^{LS}(r; \vartheta_1, \vartheta_2) = \left(\frac{D_{\diamond}(\mathbf{r}_1, \vartheta_1) D_{\diamond}(\mathbf{r}_2, \vartheta_2)}{R_{\diamond}(\mathbf{r}_1, \vartheta_1) R_{\diamond}(\mathbf{r}_2, \vartheta_2)} \right) \frac{N_R^{\diamond}(N_R^{\diamond} - 1)}{N_D^{\diamond}(N_D^{\diamond} - 1)} - \left(\frac{D_{\diamond}(\mathbf{r}_1, \vartheta_1) R_{\diamond}(\mathbf{r}_2, \vartheta_2)}{R_{\diamond}(\mathbf{r}_1, \vartheta_1) R_{\diamond}(\mathbf{r}_2, \vartheta_2)} \right) \frac{N_R^{\diamond}(N_R^{\diamond} - 1)}{N_D^{\diamond} N_R^{\diamond}} + 1 \quad (14)$$

The Ψ^N is called the "natural estimator" (Landy & Szalay 1993b). Also, the Ψ^H is proposed by Hamilton (1993) while the Ψ^{LS} introduced by Landy & Szalay (1993b) has a nearly Poisson variance. In the above equation, $D_{\diamond}(\mathbf{r}_1, \vartheta_1) D_{\diamond}(\mathbf{r}_2, \vartheta_2)$ and $R_{\diamond}(\mathbf{r}_1, \vartheta_1) R_{\diamond}(\mathbf{r}_2, \vartheta_2)$ represent the number of peak or trough pairs in the data and random catalogs, respectively. Also $D_{\diamond}(\mathbf{r}_1, \vartheta_1) R_{\diamond}(\mathbf{r}_2, \vartheta_2)$ is the number of cross-pairs. In the above equations, N_D^{\diamond} and N_R^{\diamond} are respectively the total number of local extrema in the data and random catalogs. The lower part in the Fig. 1, indicates the peak pairs separated by r in a magnified patch.

2.3 Genus Topology

Differential and algebraic topologies representing, respectively, the local and the global properties are complementary methods in examining the properties of stochastic fields (Adler 1981; Adler & Taylor 2011; Adler et al. 2010). Among different topological measures, genus topology which directly tests the Gaussianity of underlying stochastic field has been developed by Doroshkevich (1970); Adler (1981); Bardeen et al. (1986); Gott III et al. (1986); Hamilton et al. (1986); Bond & Efstathiou (1987); Coles (1988); Matsubara (1994, 1996); Matsubara & Yokoyama (1996); Matsubara (2003); Gay et al. (2012); Pranav et al. (2019).

The pioneer implementation of topology on the CMB map was done in (Coles 1988; Gott III et al. 1990). Increasing the precision of CMB data observed by different surveys encouraged different groups to apply topological measures for testing the non-Gaussianity and assessment of exotic features (Arbuzov et al. 1997; Colley & Richard Gott III 2003; Gott et al. 2007; Lew & Roukema 2008; Colley & Gott III 2015; Cole & Shiu 2018).

Mathematical description of two-dimensional genus statistics for isotropic CMB map is given by (Doroshkevich 1970; Adler 1981; Matsubara 2003):

$$G_2(\vartheta) = -\frac{1}{2} \langle \delta_D(\delta_T - \vartheta \sigma_0) \delta_D(\eta_{\phi}) | \eta_{\theta} | \xi_{\phi} \rangle \quad (15)$$

which for Gaussian CMB map becomes: $G_2^{\text{Gaussian}}(\vartheta) = e^{-\vartheta^2/2} \vartheta \sigma_1^2 / 2\sigma_0^2 (2\pi)^{3/2}$. The above equation is useful when we are interested in deriving analytical or semi-analytical formula for genus, while computational approach to determine genus of CMB map can be deduced by means of Morse

theory making a connection between Euler characteristic and critical points (Gay et al. 2012, and references therein). Subsequently, the genus for (1+2)-D field reads as:

$$G_2(\vartheta) = \text{number of hot spots} - \text{number of cold spots} \quad (16)$$

We will compute G_2 for both semi-Planck simulation data sets and different Planck component separations. Subsequently, the statistical reliability of probable non-Gaussianity will be examined.

2.4 General definition of bias factor

General statistical expression for the relation between unweighted TPCF as excess probability of finding a typical feature and the weighted TPCF which is known as autocorrelation function, in the first order of approximation reveals a linear and scale-independent bias factor. For a Gaussian random field, the excess probability of finding pairs of sharp clipping is statistically magnified by the fluctuation of random field for long distance (angle) separation at high threshold, $\vartheta \gg 1$. In this regime, we have $\Psi_{pix-pix}(\theta; \vartheta) \sim e^{\mathcal{B}_{pix}^2(\vartheta) C_{TT}(\theta)} - 1$ with $\mathcal{B}_{pix}(\vartheta) \sim \vartheta$ (Kaiser 1984; Taquu 1977; Politzer & Wise 1984; Jensen & Szalay 1986; Bardeen et al. 1986; Szalay 1988b,c) (for extensive discussion see (Martinez & Saar 2001; Desjacques et al. 2018, and references therein)).

Now, we turn to the modulation of local maxima number density at threshold ϑ in the CMB map by the temperature fluctuations at the last scattering surface. In another word, we look for the relation between unweighted TPCF of peaks and weighted TPCF of temperature fluctuations. The general form of bias factor enables us to estimate unweighted TPCF of typical feature by weighted TPCF, which is more simple to compute. Generally, we expect that the number density of peaks is enhanced where the temperature fluctuations are high. For CMB map, we define peaks number density contrast as: $\delta_{pk} \equiv \frac{n_{pk} - \langle n_{pk} \rangle}{\langle n_{pk} \rangle}$. For determining the scale-independent bias factor averaged on all peak curvature values, we are interested in examining such relation $\delta_{pk} = \mathcal{B}_{pk}(\vartheta) \delta_T$. Following Kaiser (1984) for sharp clipping statistics, we exploit a systematic relation between unweighted TPCF of local extrema, $\Psi_{\diamond-\diamond}(\theta; \vartheta_1, \vartheta_2)$, and weighted TPCF of temperature fluctuations, $C_{TT}(\theta)$, for separation angle, θ , in analogy with

$\Psi_{\circ-\circ}(\theta; \vartheta) = \mathcal{B}_{\circ}^2(\vartheta)C_{TT}(\theta)$, when we ignore the scale-dependent part. Mentioned relation is satisfied for large angle separation angle. For very high threshold value, the pixel above threshold can delineate the peak better than small threshold and consequently, we obtain $\mathcal{B}_{pk}(\vartheta) \sim \mathcal{B}_{pix}(\vartheta)$ for large enough separation angle in a Gaussian field (Martinez & Saar 2001). To examine the scale-dependent part of bias for peak statistics, we rely on a more general model for bias in the Fourier space as: $\mathcal{B}_{pk}(k, \vartheta) = \mathcal{B}_{pk}(\vartheta) + \mathcal{B}_k^{pk}(\vartheta)k^2$. Here k represents the wavelength of typical mode. It turns out that for either $\vartheta \gg 1$ or large scale, the value of scale-dependent part of bias is $\mathcal{B}_k^{pk}(\vartheta) \rightarrow 0$ (Desjacques et al. 2010, 2018). We define $\mathcal{B}_{\circ}^2(\theta, \vartheta) \equiv \Psi_{\circ-\circ}(\theta; \vartheta)/C_{TT}(\theta)$ for proper range of θ . Subsequently, any features existed in $\mathcal{B}_{\circ}^2(\theta, \vartheta)$ versus θ for a typical value of ϑ represents the contribution of the scale in this type of bias factor.

3 DATA DESCRIPTION AND SIMULATION

The *Planck* sky observational data sets contain full-sky maps at nine frequency channels for intensity of temperature and for polarization fluctuations. Throughout this paper we only focus on temperature field. Mentioned data sets have been provided in HEALPix format (Gorski et al. 2005)² represented by N_{side} parameter and convolved by a Gaussian beam. The maps can be downgraded to the lower resolution, if required, by reducing the N_{side} . We follow same algorithm explained in Ade et al. (2016c) and use $N_{\text{side}} = 2048, 1024$ and 512 from high to low resolution, respectively. To take into account the contribution of frequency-dependency in our analysis, we consider the foreground cleaned version of the 100, 143 and 217 GHz maps (Ade et al. 2014a).

The CMB maps produced by *Planck* team are based on different component separation algorithms, namely Commander-Ruler (CR), NILC, SEVEM and SMICA (Ade et al. 2014b). Such component separation algorithms enable us to achieve the largest possible sky area coverage. In addition, these procedures can remove galactic emission and reconstruct the diffuse emission from our galaxy (see Dickinson (2016) for a comprehensive description on CMB foreground). The proper mask and the corresponding fraction of unmasked pixels used for CMB data are specified by UT78 and $f_{\text{sky}} = 77.6\%$, respectively (Ade et al. 2016c). To realize reliable statistical inferences about the number density of the local extrema and associated clustering, we also need fiducial simulations as the reference sets and for debiasing in our statistical analysis. To this end, we use 100 realizations of the Full Focal Plane LFI-143 GHz maps (Ade et al. 2016a) and they are publicly available on Planck Legacy Archive³. The Full Focal Plane fiducial CMB power spectrum is based on Λ CDM model with the best-fit *Planck* parameters (Aghanim et al. 2016). To interpret our results, the fiducial maps would be the Gaussian-based expectation.

² <http://healpix.sourceforge.net>

³ <https://pla.esac.esa.int/pla/#maps>

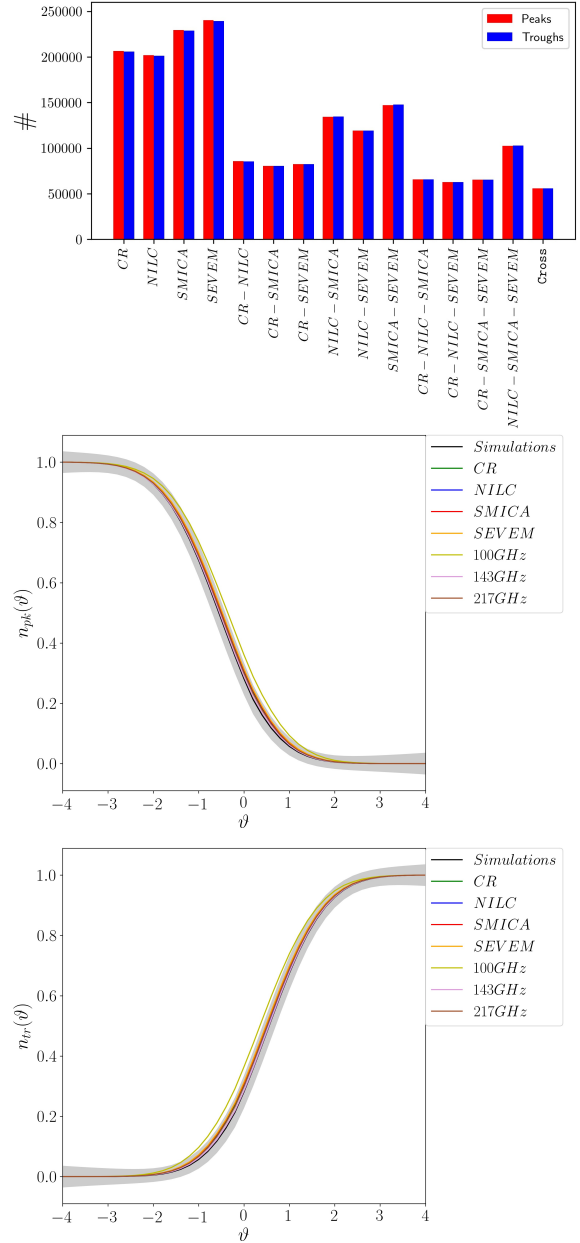


Figure 2. Upper panel: Total number of local extrema (peaks (light color) and troughs (dark color)) for different CMB separation components and cross-combination maps. Middle panel: Cumulative number density of peaks above a threshold. Lower panel: Cumulative number density of troughs below a threshold. The shaded region corresponds to the 1σ optimal variance error determined by fiducial Gaussian CMB map. We considered $N_{\text{side}} = 2048$.

4 IMPLEMENTATION ON REAL DATA AND SYNTHETIC DATA SETS

In this section we apply our statistical measures based on critical sets explained in section 2 on *Planck* CMB maps.

4.1 Local extrema statistics of CMB map

Critical regions among of excursion sets are the efficient measures to recognize exotic features in the CMB maps. To start,

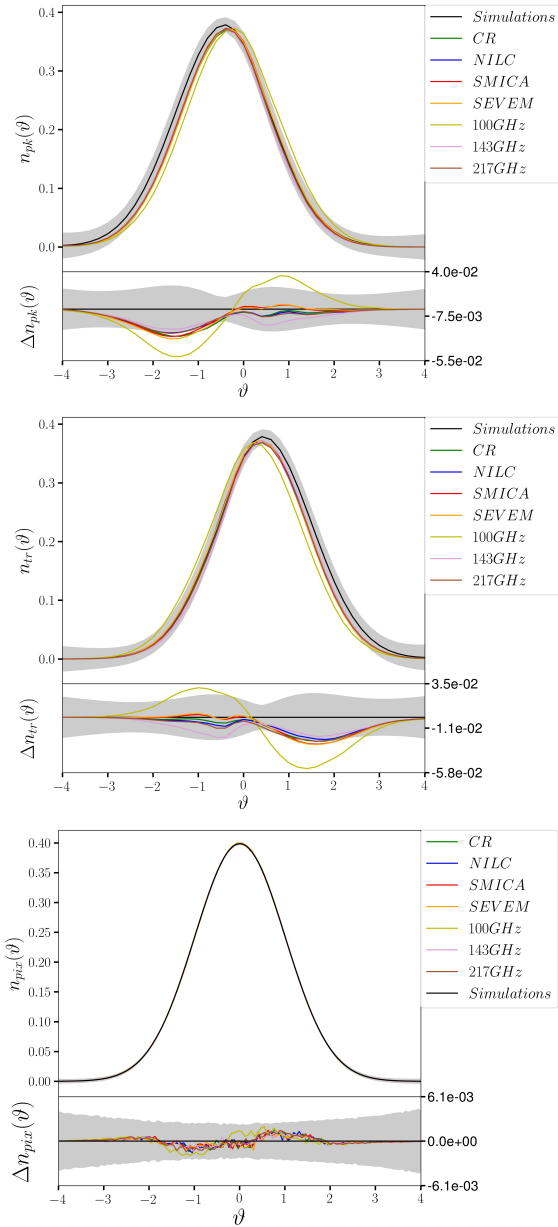


Figure 3. Number density of peaks (*upper panel*) and troughs (*middle panel*) as a function of threshold for *Planck* data sets and Gaussian simulation. The number density of pixel at the threshold is illustrated in the lower panel. In the lower part of each plot, we have computed the difference of number density with simulated map. The shaded region corresponds to the 1σ optimal variance error determined by fiducial Gaussian CMB map. The shaded region corresponds to the 1σ optimal variance error determined by fiducial Gaussian CMB map. We considered $N_{\text{side}} = 2048$.

we turn to one-point statistics of sharp clipping and local extrema. The latter is complicated due to the conditions required for extrema, while the former is more slightly less sensitive to search probable exotic features. The upper panel of Fig. 2 illustrates the total number of peaks and troughs for various component separation methods.

We also introduce a new local extrema map (**Cross map**) using extrema point validated by cross-combination

of all available component separations. This method determines almost real local extrema and removes fake peaks and troughs caused by systematic and undesired sources. Our results demonstrate that all types of *Planck* CMB maps have unresolved shot noises while the cross-combination shows a considerable reduction in the number of local extrema. Therefore, those analysis based on such kinds of excursion sets essentially lead to intrinsic bias. The middle panels of Fig. 2 shows the normalized cumulative number density of local maxima, while lower panel illustrates the cumulative number density of trough below the threshold. As indicated in this plot, all component separations with different frequency bands are consistent with Gaussian field represented by simulation. However the *Planck* 100 GHz map has excess value for normalized cumulative peaks for $\vartheta > 0$ and therefore an excess value for troughs is found for $\vartheta < 0$. The shaded area around each curve represents the 1σ statistical level of confidence.

Fig. 3 depicts the number density of local maxima (upper panel), local minima (middle panel) and pixel at the threshold (lower panel). Among different types of data, the *Planck* 100 GHz series shows a deviation from Gaussian prediction. Since other maps are consistent with the Gaussian prediction at 1σ confidence, the deviation in the *Planck* 100 GHz can not be a signature for the primordial non-Gaussianity. In addition, taking into account the cross-combination between all components makes the result to be more consistent with Gaussian field. Another interesting result is that, there is no significant difference between $n_{pk}(\vartheta)$ and $n_{tr}(-\vartheta)$ for all of CMB maps, as expected for a Gaussian field. The sharp clipping statistics is less sensitive to non-Gaussianity (lower panel of Fig. 3).

Going beyond the one-point statistics of critical sets provides a proper opportunity for examining exotic features and manipulating artificial contributions from undesired non-cosmological sources. We check all the estimators introduced by Eqs. (12), (13) and (14). Our analysis demonstrates that all results are consistent with each others and therefore for the rest of this paper, we will show what we have obtained by Hamilton estimator (Eq. (13)). We find all the peaks and troughs above thresholds in the interval corresponds to $-3 \leq \vartheta \leq 3$ with step size 0.5 in each full sky simulated map and then apply unweighted TPCF estimator to compute $\Psi_{\diamond-\diamond}(\theta; \vartheta)$ for both observed and simulated maps. The final results are given by ensemble averaging over all realizations. Such results play the role of numerical results for the Gaussian map. Unweighted TPCF of peaks as a function of separation angle indicates in Fig. 4 for *Planck* data above a given threshold for different component separation algorithms and various frequency channels. To examine the contribution of unresolved shot and systematic noises in the $\Psi_{\diamond-\diamond}$, we compute unweighted TPCF of peaks for different cross-combination maps represented by two names in each plots of Fig. 4. Our results confirm non-Gaussianity for small scale, $\theta \lesssim 15'$. By increasing the threshold value and considering cross-combinations in presenting peaks, non-Gaussianity decreases. We also assess the unweighted TPCF of peaks for $\delta_T < -\vartheta\sigma_0$ and for $\delta_T > +\vartheta\sigma_0$. For an ideal Gaussian random field, we expect to have $\Psi_{\diamond-\diamond}(\delta_T < -\vartheta\sigma_0) = \Psi_{\diamond-\diamond}(\delta_T > +\vartheta\sigma_0)$ due to symmetry between peaks and troughs. Our results confirm that observed CMB data are consistent with this expectation. While

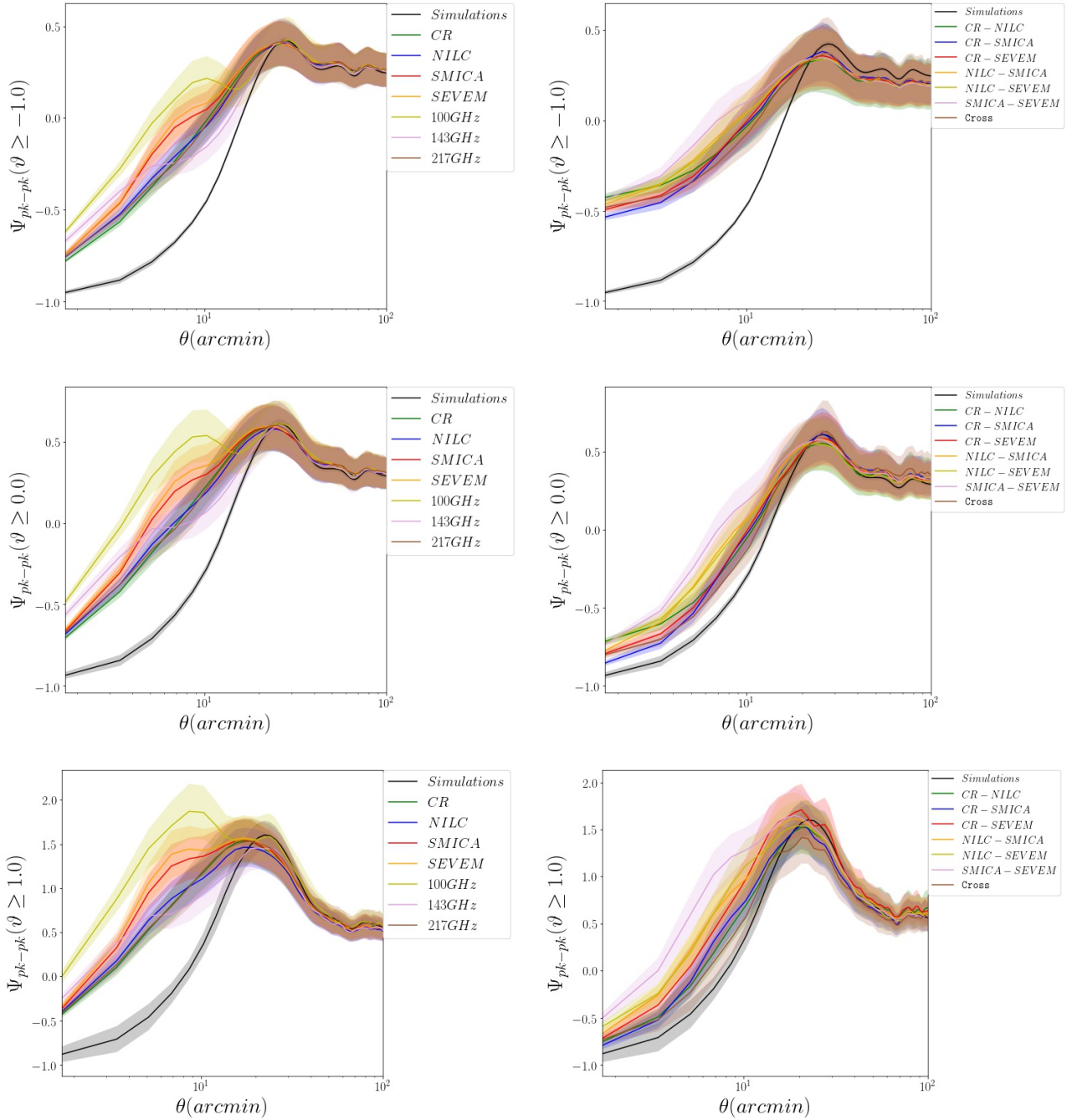


Figure 4. *Upper left panel:* Unweighted TPCF of peaks in the CMB maps above $\vartheta \geq -1.0$. *Upper right panel:* Unweighted TPCF of local maxima for $\vartheta \geq -1.0$ when we take into account the cross-combination maps. *Middle left panel:* Unweighted TPCF of peaks in CMB maps above $\vartheta \geq 0.0$. *Middle right panel:* TPCF of local maxima for $\vartheta \geq 0.0$ when we take into account the cross-combination maps. *Lower left panel:* TPCF of peaks in the CMB maps above $\vartheta \geq +1.0$. *Lower right panel:* Unweighted TPCF of local maxima for $\vartheta \geq +1.0$ when we take into account the cross-combination maps. Simulation in this plot corresponds to Λ CDM Gaussian CMB simulated map. The shaded region corresponds to the 1σ optimal variance error determined by fiducial Gaussian CMB map. We considered $N_{\text{side}} = 2048$.

for clustering of the pixels above and below a threshold for WMAP data done by Rossi et al. (2009), showed different results for large angle separation. This achievement clarifies that peak-peak statistics rather than pixel-pixel analysis is more robust in the presence of un-resolve noises.

The position of so-called bump for unweighted TPCF

of peaks above a given threshold versus ϑ is indicated in the upper panel of Fig. 5. Lower panel corresponds to the value of unweighted TPCF of peaks around *Doppler peak*, $\theta \sim 75'$ as a function of threshold. According to the semi-analytical approach (see Heavens & Sheth (1999)), by increasing the threshold, the unweighted TPCF of peaks in a

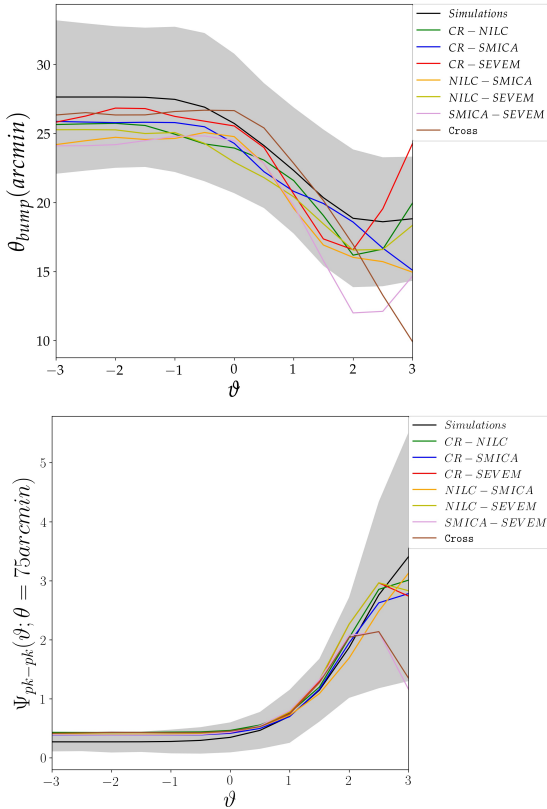


Figure 5. *Upper panel:* The value of angular separation at which, unweighted TPCF of peaks reaches to its maximum value (θ_{bump}) as a function of threshold. *Lower panel:* The value of unweighted TPCF of peaks around *Doppler peak*, $\theta \sim 75'$ as a function of threshold. Simulation in this plot corresponds to Λ CDM Gaussian CMB map. The shaded region corresponds to the 1σ optimal variance error determined by fiducial Gaussian CMB map. Here we considered $N_{side} = 2048$.

Gaussian CMB map reaches to its maximum value for lower separation angle. Such behavior can be justified by means of the distribution of local maxima at higher threshold which is more distinguishable from random catalog. Applying the different beam size can also wash out the peaks and suppressing the bump in Ψ for all thresholds (Heavens & Sheth 1999).

According to researches done by Takada et al. (2000); Takada & Futamase (2001), the bump and main trough around *Doppler peak* in unweighted TPCF of peaks are more sensitive to the effect of gravitational lensing on the CMB photons which are randomly deflected by foreground ranging from large scale structures to cosmic strings networks. In other word, redistribution of peak in the CMB map from intrinsic separation and distribution by weak lensing phenomenon have unique signature on $\Psi_{\diamond-\diamond}$. The contribution of weak lensing on the $\Psi_{\diamond-\diamond}$ leads to mitigate the depth of *Doppler peak* and even suppressing the maximum value of Ψ as a function of separation angle Takada & Futamase (2001). To put proper constraint on the amplitude of the mass fluctuations, we need more deep troughs around $\theta \approx 70' - 75'$, consequently, according to Fig. 4, we should compute $\Psi_{\diamond-\diamond}$ for $\vartheta \gtrsim +1.0$ due to more compatibility between different

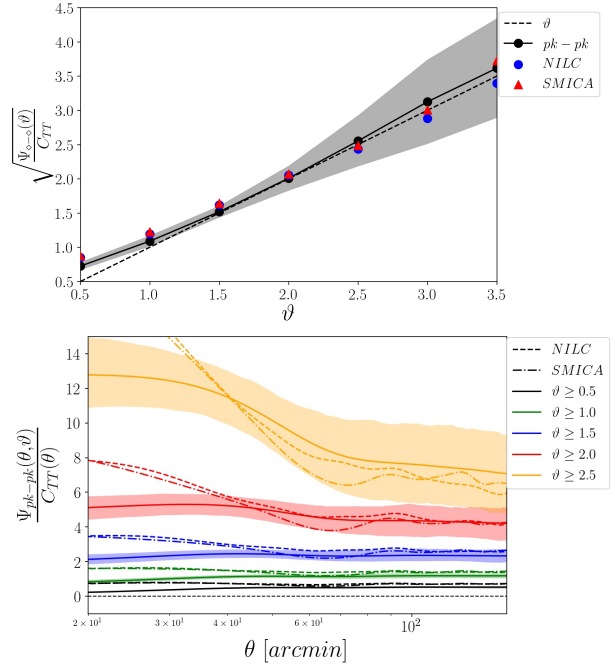


Figure 6. *Upper panel:* Scale-independent bias factor for peaks above threshold for CMB simulated data and *Planck* maps. The dashed line shows the results for pixels above a threshold given by theory for Gaussian field while the filled circle symbol with line is for peaks above threshold for simulated CMB map. Others symbols indicate the results for NILC and SMICA maps. *Lower panel:* Evaluation of scale-dependent bias for peak statistics above a threshold for NILC (dashed line), SMICA (dashed-dot line) and CMB simulated maps (solid line). The shaded region corresponds to the 1σ optimal variance error determined by fiducial Gaussian CMB map. By increasing both angle separation and threshold value, the consistency with $\mathcal{B}_{pk}^2 \sim \vartheta^2$ increases.

separation components of CMB achieved for higher thresholds around *Doppler peak*.

The upper panel of Fig. 6 indicates the scale independent bias factor for peaks above a threshold for CMB observed and simulated data sets. Here, we average on the ratio of Ψ_{pk-pk}/C_{TT} for large enough separation angle for each threshold denoted by symbols. For a Gaussian stochastic field, we expect to have $\mathcal{B}_{pix}(\vartheta) \sim \vartheta$, for high threshold (Kaiser 1984; Taqqu 1977; Politzer & Wise 1984; Jensen & Szalay 1986; Bardeen et al. 1986; Szalay 1988b,c). Semi-analytical investigation at very high threshold clarifies that, peak and pixel statistics become identical and our results are compatible with this issue.

To examine the contribution of angular scale in the bias, we compute $\mathcal{B}_{pk}(\theta, \vartheta)$ as a function of θ for some typical thresholds. The lower panel of Fig. 6 illustrates the unweighted TPCF of peaks to correlation function of temperature fluctuations ratio, versus scale for various thresholds. In this panel the solid lines correspond to the Gaussian CMB simulated maps, while dashed and dashed-dot lines correspond to NILC and SEVEM, respectively. The presence of some features particularly in the angular scale interval, $20' \lesssim \theta \lesssim 80'$, confirms that for small scale, the footprint of scale essentially appears in the bias factor, while for large enough separation angle, such features are diminished. In the

latter regime and for $\vartheta \gg 1$, we expect to have a plateau for \mathcal{B}^2 and its value is proportional to ϑ^2 . It is worth mentioning that, the results for *Planck* data sets are compatible with that of expected for Gaussian field, while for small scales, we have some deviations from results for simulated map. By increasing the threshold, the consistency between *Planck* data and simulations increases.

4.2 Testing Gaussian Hypothesis

Non-Gaussianity in the CMB data can be produced by late phenomena such as gravitational lensing, Sunyaev-Zel'dovich effect, contaminations from foreground and residual point sources. Primordial non-Gaussianity can be generated by a sequence of phase transitions and deviation from un-correlated initial fluctuations during the inflationary epoch (Komatsu 2002; Lewis & Challinor 2006; Ade et al. 2014c; Lewis et al. 2016).

To probe hypothesis of Gaussianity, many statistical approaches have been proposed (Heavens & Sheth 1999; Tojeiro et al. 2006; Rossi et al. 2009, 2011; Ade et al. 2014c; Lewis et al. 2016; Novaes et al. 2016; Cole & Shiu 2018, and references therein). Here we implement clustering of local extrema to evaluate the Gaussianity of *Planck* CMB maps with different resolutions. We degrade observed maps with original $N_{\text{side}} = 2048$ to other resolutions represented by $N_{\text{side}} = 1024, 512, 256, 128$ using degraded common mask UT76 (Ade et al. 2016c). In our analysis, we utilize 100 Full Focal Plane full-sky simulated Gaussian maps (Ade et al. 2016a). For a Gaussian stochastic field, $\mathcal{P}(\mathcal{A}_{\mu 1}; \mathcal{A}_{\mu 2})$ is modeled by the Gaussian multivariate function. Any deviation from Gaussianity is encoded in joint PDF leading to a deviation in unweighted TPCF from a typical Gaussian model. Therefore, this quantity is a powerful measure for testing Gaussian hypothesis (Heavens & Sheth 1999; Rossi et al. 2009).

Based on an efficient estimator for local extrema clustering introduced by Eq. (13)⁴, we compute $\Psi_{\diamond-\diamond}^{\text{sim}}(\theta; \vartheta)$ for a given threshold, ϑ , for simulated maps. Here \diamond can be replaced by "pk" for local maxima above a given threshold or "tr" for local minima below a given threshold. Each computed $\Psi_{\diamond-\diamond}^{\text{sim}}(\theta; \vartheta)$ for a given threshold is divided into 25 classes for separation angle in the range of $\theta \in [5' - 100']$ and finally we record corresponding values in an array. Relying on computed results for $\Psi_{\diamond-\diamond}^{\text{sim}}(\theta; \vartheta)$, we make covariance matrix $\mathcal{C}_{\diamond-\diamond}$ with size 25×25 . In order to determine the significance of deviation from Gaussian hypothesis, following chi-square is computed for various data sets either simulated maps or different component separations of *Planck* data sets as:

$$\chi_{\diamond-\diamond}^2(\vartheta, i) = \frac{[\Psi_{\diamond-\diamond}(\vartheta, i) - \langle \Psi_{\diamond-\diamond}^{\text{sim}}(\vartheta, j) \rangle_j]^\dagger}{\mathcal{C}_{\diamond-\diamond}^{-1}(\vartheta)} [\Psi_{\diamond-\diamond}(\vartheta, i) - \langle \Psi_{\diamond-\diamond}^{\text{sim}}(\vartheta, j) \rangle_j] \quad (17)$$

here $j = 1, \dots, 100$ for simulated map and $i = 1, \dots, 5$ for different component separations, namely CR, NILC,

⁴ We have also carried out other estimators represented by Eqs. (13) and (14) for some of our analysis and derived results were consistent to each others

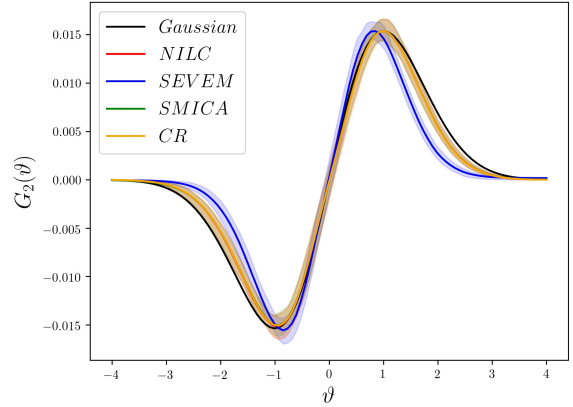


Figure 7. Genus topology for *Planck* CMB maps. The theoretical prediction is represented by thin solid line for the Gaussian CMB map. The shaded region corresponds to the 1σ optimal variance error determined by fiducial Gaussian CMB map. We considered $N_{\text{side}} = 2048$.

SMICA, SEVEM and Cross maps. Also $\mathcal{C}_{\diamond-\diamond, mn}(\vartheta) \equiv \langle [\Psi_{\diamond-\diamond}^{\text{sim}}(\theta_m; \vartheta, i) - \langle \Psi_{\diamond-\diamond}^{\text{sim}}(\theta_m; \vartheta, j) \rangle_j] [\Psi_{\diamond-\diamond}^{\text{sim}}(\theta_n; \vartheta, i) - \langle \Psi_{\diamond-\diamond}^{\text{sim}}(\theta_n; \vartheta, j) \rangle_j] \rangle_i$. We compute probability density function of $\chi_{\diamond-\diamond}^2(\vartheta, i)$ for Gaussian simulated map, $P(\chi_{\diamond-\diamond}^2(\vartheta))$. Accordingly, for each observed data sets, we compute $P(\chi^2 > \chi_{\diamond-\diamond}^2(\vartheta))$, namely probability for having a typical value for χ^2 larger than the one measured for observed map. Table 1 shows the $P(\chi^2 > \chi_{\diamond-\diamond}^2(\vartheta))$ for clustering of peaks and troughs for different thresholds. The SMECA map indicates a deviation for clustering of peaks for $\vartheta \geq 1.0$ from Gaussian prediction. Since other components do not show meaningful deviation, therefore this result is not reliable from statistical point of view.

We repeat same analysis for different degraded maps, namely, $N_{\text{side}} = 2048, 1024$ and 512 . Table 2 reports the P-value for deviation of our results based on $\Psi_{pk-pk}(\vartheta \geq 0.0)$. Decreasing the resolution results in obtaining more consistency with Gaussian hypothesis. Our results demonstrate that, there is no significant evidence for Gaussian hypothesis rejection.

The genus topology of *Planck* data is indicated in Fig. 7. As illustrated by this figure, the G_2 as a function of threshold for SEVEM has a deviation from that of predicted for Gaussian field. But other type of map are consistent with Gaussian genus function.

4.3 Asymmetry in clustering of local extrema

In order to examine the probable asymmetry superimposed on the observational data sets in the context of Gaussianity property, we calculate n_{\diamond} and $\Psi_{\diamond-\diamond}$ for all 3072 un-masked disks with size 6° centered on the pixels of a HEALPix $N_{\text{side}} = 16$ (Gorski et al. 2005). Therefore, we represent our measures for each direction in each simulation as: $n_{\diamond}(\vartheta, j, i)$ and $\Psi_{\diamond-\diamond}(\theta_m; \vartheta, j, i)$ in which, $m = 1, \dots, 25$ corresponds to the label of separation angle bin, $j = 1, \dots, 3072$ represents the number of non-overlapped disk and $i = 1, \dots, 100$ indicates the label of simulated map. While for observed map, we have $i = 1, \dots, 5$ corresponding to the different component separation maps. Based on number density of local extrema,

Table 1. The $P(\chi^2 > \chi_{\diamond-\diamond}^2(\vartheta))$ for quantifying null hypothesis of Gaussianity accepting for various observed maps. Here we consider $N_{\text{side}} = 2048$.

Map/Probability	$P(\chi^2 > \chi_{pk-pk}^2(\vartheta \geq 0.0))$	$P(\chi^2 > \chi_{pk-pk}^2(\vartheta \geq 1.0))$	$P(\chi^2 > \chi_{tr-tr}^2(\vartheta \leq 0.0))$	$P(\chi^2 > \chi_{tr-tr}^2(\vartheta \leq -1.0))$
Cross.....	0.15	0.69	0.18	0.12
CR.....	0.23	0.50	0.76	0.44
NILC.....	0.46	0.40	0.93	0.74
SMICA.....	0.20	0.08	0.90	0.90
SEVEM.....	0.20	0.34	0.96	0.99

Table 2. The $P(\chi^2 > \chi_{pk-pk}^2(\vartheta \geq 0.0))$ for quantifying null hypothesis of Gaussianity accepting for various observed maps.

Map/ N_{side}	2048	1024	512
Cross.....	0.83	0.86	0.91
CR.....	0.87	0.98	0.99
NILC.....	0.98	1.0	0.93
SMICA.....	0.46	0.97	1.0
SEVEM.....	0.95	0.96	0.98

we compute $\langle n_{\diamond}^{\text{sim}}(\vartheta, j, i) \rangle_i$. The significance of difference between $n_{\diamond}(\vartheta, j, i)$ for each patch in each observed map can be derived by P-value statistics. Table 3 shows the minimum value of P-value for peaks and troughs for different thresholds. Our results show almost a significant deviation from isotropic field when we use, peak statistics at $\vartheta \geq 0.0$ and for trough measure at $\vartheta \leq 0.0$. Mentioned values happened for different patches. To get the meaningful probable asymmetry, we utilize another posterior covariance analysis to determine the statistical significance of amount asymmetry represented by one-point statistics of local extrema.

The χ^2 for unweighted TPCF is given by:

$$\chi_{\diamond-\diamond}^2(\vartheta, j, i) = \frac{[\Psi_{\diamond-\diamond}(\vartheta, j, i) - \langle \Psi_{\diamond-\diamond}^{\text{sim}}(\vartheta, j, i) \rangle_i]^{\dagger}}{C_{\diamond-\diamond}^{-1}(\vartheta, j)} \frac{[\Psi_{\diamond-\diamond}(\vartheta, j, i) - \langle \Psi_{\diamond-\diamond}^{\text{sim}}(\vartheta, j, i) \rangle_i]}{(18)}$$

here $C_{\diamond-\diamond, mn}(\vartheta, j) \equiv \langle [\Psi_{\diamond-\diamond}^{\text{sim}}(\theta_m; \vartheta, j, i) - \langle \Psi_{\diamond-\diamond}^{\text{sim}}(\theta_m; \vartheta, j, i) \rangle_i][\Psi_{\diamond-\diamond}^{\text{sim}}(\theta_n; \vartheta, j, i) - \langle \Psi_{\diamond-\diamond}^{\text{sim}}(\theta_n; \vartheta, j, i) \rangle_i] \rangle_i$ for each threshold and each direction. The probability density function of $\chi_{\diamond-\diamond}^2(\vartheta, j, i)$ for Gaussian simulated map will be computed and we determine $P(\chi^2 > \chi_{\diamond-\diamond}^2(\vartheta, j, i))$ for j th disk in i th observed map. Table 4 shows the minimum value of $P(\chi^2 > \chi_{\diamond-\diamond}^2(\vartheta))$ for clustering of peaks and troughs for different thresholds. We also compute the weighting averaged over separation angle of peak clustering in each disk for observed maps represented by $\langle \Psi_{pk-pk}(\theta; \vartheta, i) \rangle_{\theta}$. Then the corresponding fluctuations of mentioned measure with respect to the 5 types of observed maps, $\sigma_{pk}(\vartheta, j)$ will be computed. Fig 8 shows $\sigma_{pk}(\vartheta \geq 1.0)$ for all available patches. However, we have some disks with high variances, but by repeating same calculation for other thresholds and even for other type of measures, we obtain threshold dependent results yielding non-physical reason for finding such preferred direction. Our results confirm the consistency with isotropic Gaussian hypothesis.

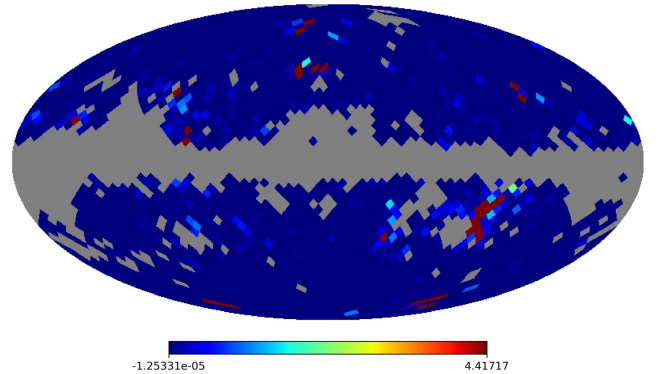


Figure 8. The Mollweide projection of disk patches with size 6° in diameter containing the $\sigma_{pk}(\vartheta \geq 1.0)$ for patches computed for SMICA.

4.4 Cosmic String Network Detection

A series of phase transitions can be taken place at the very early Universe and meanwhile depending on topology of potential of underlying field, we expect to obtain point-like (mono-pole), line-like (cosmic string (CS)) and texture of topological defects due to spontaneous symmetries in expanding and cooling the Universe (Kibble 1976, 1980; Hindmarsh & Kibble 1995; Vilenkin & Shellard 2000; Copeland & Kibble 2010; Polchinski 2005). Particularly, CS network is predicted to be existed by hybrid inflation, brane-world and superstring theories (Kibble 1976; Zeldovich 1980; Vilenkin 1981; Vachaspati & Vilenkin 1984; Vilenkin 1985; Shellard 1987; Hindmarsh & Kibble 1995; Vilenkin & Shellard 2000; Sakellariadou 2007; Bevis et al. 2008; DePies & Hogan 2007; Bevis et al. 2010; Copeland et al. 1994; Sakellariadou 1997; Sarangi & Tye 2002; Copeland et al. 2004; Pogosian et al. 2003; Majumdar & Christine-Davis 2002; Dvali & Vilenkin 2004; Kibble 2004; Henry Tye 2008). The energy density characterization of CS is given by string tension: $\frac{G\mu}{c^2} = \mathcal{O}\left(\frac{\varpi^2}{M_{\text{Planck}}^2}\right)$. Here $M_{\text{Planck}} \equiv \sqrt{\hbar c/G}$ is the Planck's mass, c indicates the speed of light and ϖ is the energy of symmetry breaking scale. The search for the footprint of CS network leads to find proper bounds on the $G\mu$ (see Ade et al. (2014d); Vafaei Sadr et al. (2017, 2018) and references therein).

To find the upper bound on the CS's tension in *Planck* data using the local extrema clustering approach, at first, we follow same recipe for simulation CS-induced CMB map as discussed by Bennett & Bouchet (1990); Ringeval et al.

Table 3. The P-value for accepting null hypothesis of asymmetry in the context of non-Gaussianity of number density of local maxima and minima. The higher value of probability, the higher probability of consistency with an isotropic map.

Map/Measure	$\langle n_{pk} \rangle (\vartheta \geq 0.0)$	$\langle n_{pk} \rangle (\vartheta \geq 1.0)$	$\langle n_{tr} \rangle (\vartheta \leq -1.0)$	$\langle n_{tr} \rangle (\vartheta \leq 0.0)$
Cross.....	0.02	0.70	0.87	0.19
CR.....	0.45	0.89	0.95	0.46
NILC.....	0.48	0.90	0.51	0.81
SMICA.....	0.35	0.89	0.96	0.42
SEVEM.....	0.46	0.93	0.98	0.48

Table 4. The value of probability for accepting null hypothesis of asymmetry in the context of non-Gaussianity of local maxima and minima clustering. The higher value of probability, the higher probability of consistency with an isotropic map.

Map/Probability	$P(\chi^2 > \chi_{pk-pk}^2(\vartheta \geq 0.0))$	$P(\chi^2 > \chi_{pk-pk}^2(\vartheta \geq 1.0))$	$P(\chi^2 > \chi_{tr-tr}^2(\vartheta \leq -1.0))$	$P(\chi^2 > \chi_{tr-tr}^2(\vartheta \leq 0.0))$
Cross.....	0.51	0.34	0.41	0.26
CR.....	0.41	0.53	0.79	0.68
NILC.....	0.44	0.55	0.70	0.74
SMICA.....	0.60	0.62	0.97	1.0
SEVEM.....	0.83	0.76	0.95	1.0

(2007); Fraisse et al. (2008); Vafaei Sadr et al. (2017, 2018). We use high-resolution flat-sky CMB maps extended for large redshift interval by map stacking method Bouchet et al. (1988); Ringeval & Bouchet (2012). The CS tensions used in this work are in the range $2.6 \times 10^{-11} \leq G\mu \leq 5.0 \times 10^{-7}$ classified into 18 classes for each simulation category. For a given $G\mu$, we compute the covariance matrix as: $C_{\vartheta-\vartheta, mn}(G\mu, \vartheta) \equiv \langle [\Psi_{\vartheta-\vartheta}^{\text{sim}}(\theta_m; G\mu, \vartheta, i) - \langle \Psi_{\vartheta-\vartheta}^{\text{sim}}(\theta_m; G\mu, \vartheta, i) \rangle] [\Psi_{\vartheta-\vartheta}^{\text{sim}}(\theta_n; G\mu, \vartheta, i) - \langle \Psi_{\vartheta-\vartheta}^{\text{sim}}(\theta_n; G\mu, \vartheta, i) \rangle] \rangle$, and $\chi_{\vartheta-\vartheta}^2(G\mu, \vartheta, i)$. Now for observed map, we also determine corresponding $\chi_{\vartheta-\vartheta}^2(\vartheta, i)$. Finally we compare the observation and simulations by checking the inequality as $0.05 \geq \int_{\chi^2 > \chi_{pk-pk}^2(\vartheta)} P(\chi^2(G\mu, \vartheta)) d\chi^2(G\mu, \vartheta)$. We expect that for higher/lower value of $G\mu$, we obtain lower/higher P-value. Therefore, the minimum value of $G\mu$ for which the mentioned inequality is satisfied will be considered by the upper value of CS tension recognized in the observations.

In this research, we compare $\Psi_{pk-pk}(\vartheta \geq 0)$ computed for different observations and the one computed for various $G\mu$ simulations. We report the $G\mu^{(\text{up})}$ for $\vartheta \geq 0.0$ in Table 5. Comparing our upper bound on CS tension with that of reported by *Planck* team confirms that taking into account the local extrema leads to higher upper bound. This is due to unresolved shot noises. To reduce this effect, we consider the cross-combination of all component separations. Our results obviously leads to the lower value for $G\mu$ in observation. The value of upper bound on Cs's tension is $G\mu^{(\text{up})} \leq 5.00 \times 10^{-7}$ for Cross map.

5 SUMMARY AND CONCLUSIONS

CMB map as a (1+2)-D stochastic field includes thermodynamic temperature and two types of polarizations. Mentioned components contain useful information ranging from the early epoch to the late time era. Various physical phenomena have different footprints on the CMB map. The

Table 5. The upper bound on the tension of cosmic strings network, $G\mu^{(\text{up})}$, utilizing $\Psi_{pk-pk}(\vartheta \geq 0)$ as a criterion for recognition.

Map	$G\mu^{(\text{up})}$
Cross.....	5.00×10^{-7}
CR.....	9.29×10^{-7}
NILC.....	9.31×10^{-7}
SMICA.....	9.81×10^{-7}
SEVEM.....	9.92×10^{-7}

stochasticity nature of CMB fluctuations motivates us to rely on geometrical and topological measures to achieve deep insight through the physical mechanisms and associated evolutions. In this paper we focused on thermodynamic temperature fluctuations and we addressed the critical sets properties not only in the one-point statistics but also in the two-points analysis. After a comprehensive explorations in different researches, we turn to the robust perturbative approach to determine joint PDF of different components of CMB random field to clarify some examples of excursion and critical sets in the form of one- and two-point statistics. We particularly derived the perturbative definition of number density of pixels above a threshold up to $\mathcal{O}(\sigma_0^3)$. By means of excess probability of finding a typical feature, we computed unweighted TPCF of local extrema and we revisited the semi-analytical definition of unweighted TPCF of peaks and troughs. In practice, utilizing semi-analytical approach may encounter with finite size effect. Therefore we considered three powerful estimators for the rest part of our analysis (Eqs. (12), (13) and (14)). The genus topology for different component separation of *Planck* maps has been computed.

In order to prepare a robust framework for comparison between Gaussian prediction and that of computed for observed data sets, we considered reliable estimators for unweighted TPCF and applied them on the CMB simulated

maps (Ade et al. 2016a) and various component separations with different resolutions at different frequency bands as observed by *Planck* (Ade et al. 2014b).

One-point statistics of local extrema and sharp clipping in the form of probability density as a function of threshold and also cumulative probability density function have been computed for both simulations and observed *Planck*. Number of peaks and troughs for different observed maps indicated different results demonstrating non-resolved shot noises in different separation components. The number density of sharp clipping for different data sets were compatible with Gaussian hypothesis, while considering constraints in recognizing pixels as local extrema magnify the deviations from Gaussianity. In this case, we obtained a discrepancy between the *Planck* data for 100GHz band and Gaussian CMB map. This kind of non-Gaussianity is frequency dependent and may not have primordial origin.

Unweighted TPCF of local extrema illustrated different behavior particularly for $\theta \lesssim 15'$ with different values. While applying unweighted TPCF estimators for **Cross** map reduced this discrepancy and leading to almost same behavior for $\Psi_{\diamond-\diamond}(\theta \lesssim 15')$ for various observed map. But the deviation between results of observational data sets and Gaussian CMB map remained. Mentioned deviation decreased by increasing the threshold. The symmetry behavior for $\Psi_{\diamond-\diamond}(\delta_T \geq \vartheta\sigma_0)$ and $\Psi_{\diamond-\diamond}(\delta_T \leq \vartheta\sigma_0)$ were confirmed when we considered peaks and trough rather than pixel reported by Rossi et al. (2009) for *WMAP*. The value of θ around *Doppler peak* as a function of threshold was decreasing function. Our results demonstrated that for $\vartheta \gtrsim +1.0$ we are able to put more consistent constraint on the amplitude of the mass function according to the value of $\Psi_{\diamond-\diamond}(\theta \sim 70' - 75')$. The scale-independent bias factor for peaks above threshold at high threshold demonstrated $\mathcal{B}_{pk} \sim \vartheta$ which is compatible for sharp clipping in Gaussian regime, for *Planck* sets. The scale-dependent part of bias for peak statistics illustrated that some features in the angular scale interval $20' \lesssim \theta \lesssim 80'$. For small scales, some deviations between CMB simulated maps and Planck data have been recognized. we have some deviations from results for simulated map. The higher value of threshold implies the better consistency between observed and simulated CMB maps.

The non-Gaussianity has a contribution in unweighted TPCF of local extrema. Accordingly, we found that $\Psi_{pk-pk}(\vartheta \geq +1.0)$ for **SMICA** has a deviation from Gaussian prediction. But for the rest value of thresholds and even for other type of observed maps, there is good consistency with Gaussianity. Subsequently, this non-Gaussianity may have systematic reason instead of primordial origin. The genus topology of *Planck* maps demonstrated a consistency with Gaussian prediction. However, the G_2 as a function of threshold for **SEVEM** had a deviation from that of predicted for Gaussian field.

Asymmetry in the context of $\Psi_{\diamond-\diamond}(\theta; \vartheta)$ for patch size equates to 6° has been examined. Our approach confirmed that various observed maps are consistent with isotropic CMB map.

We also derived an upper bound on the cosmic string's tension via unweighted TPCF of peaks on *Planck* data. The higher value of $G\mu$ obtained by peak-peak statistics represented that un-resolved shot noise has almost effect of those results based on local extrema. Combining all maps and

apply our tools on only common peaks improve the upper bound on $G\mu^{(up)} \lesssim 5.00 \times 10^{-7}$.

ACKNOWLEDGEMENTS

The authors are really grateful to Ravi K. Sheth and M. Farhang for their extremely useful comments for different parts of this paper. The numerical simulations were carried out on Baobab at the computing cluster of the University of Geneva. SMSM appreciates the hospitality of HECAP section of ICTP where some part of this research were carried out. AVS has received funding from the European Union's Horizon 2020 research and innovation program under the Marie Skłodowska-Curie grant agreement No 674896 and No 690575 to visit Max Planck Institute for Physics in Munich. AVS also is grateful to Max Planck Institute for Physics in Munich, where a part of this work was completed.

APPENDIX A: COMPLEMENTARY DEFINITIONS

In this appendix we will give some complementary definitions used for computing critical sets of CMB field. The

$$\mathcal{K}^{(2)} \equiv \langle \mathcal{A} \otimes \mathcal{A} \rangle = \begin{bmatrix} \langle \delta_T^2 \rangle & \langle \delta_T \eta_\phi \rangle & \langle \delta_T \eta_\theta \rangle & \langle \delta_T \xi_{\phi\phi} \rangle & \langle \delta_T \xi_{\theta\theta} \rangle & \langle \delta_T \xi_{\phi\theta} \rangle \\ \langle \delta_T \eta_\phi \rangle & \langle \eta_\phi^2 \rangle & \langle \eta_\phi \eta_\theta \rangle & \langle \eta_\phi \xi_{\phi\phi} \rangle & \langle \eta_\phi \xi_{\theta\theta} \rangle & \langle \eta_\phi \xi_{\phi\theta} \rangle \\ \langle \delta_T \eta_\theta \rangle & \langle \eta_\theta \eta_\phi \rangle & \langle \eta_\theta^2 \rangle & \langle \eta_\theta \xi_{\phi\phi} \rangle & \langle \eta_\theta \xi_{\theta\theta} \rangle & \langle \eta_\theta \xi_{\phi\theta} \rangle \\ \langle \delta_T \xi_{\phi\phi} \rangle & \langle \xi_{\phi\phi} \eta_\phi \rangle & \langle \xi_{\phi\phi} \eta_\theta \rangle & \langle \xi_{\phi\phi}^2 \rangle & \langle \xi_{\phi\phi} \xi_{\theta\theta} \rangle & \langle \xi_{\phi\phi} \xi_{\phi\theta} \rangle \\ \langle \delta_T \xi_{\theta\theta} \rangle & \langle \xi_{\theta\theta} \eta_\phi \rangle & \langle \xi_{\theta\theta} \eta_\theta \rangle & \langle \xi_{\theta\theta} \xi_{\phi\phi} \rangle & \langle \xi_{\theta\theta}^2 \rangle & \langle \xi_{\theta\theta} \xi_{\phi\theta} \rangle \\ \langle \delta_T \xi_{\phi\theta} \rangle & \langle \xi_{\phi\theta} \eta_\phi \rangle & \langle \xi_{\phi\theta} \eta_\theta \rangle & \langle \xi_{\phi\theta} \xi_{\phi\phi} \rangle & \langle \xi_{\phi\theta} \xi_{\theta\theta} \rangle & \langle \xi_{\phi\theta}^2 \rangle \end{bmatrix} \quad (\text{A1})$$

The non-zero elements of $\mathcal{K}^{(2)}$ for separation angle, $\cos(\psi) = |\hat{n}_i \cdot \hat{n}_j| = 1$ are as follows (Bond & Efstathiou 1987):

$$\begin{aligned} \sigma_0^2 &\equiv \langle \delta_T^2 \rangle = \sum_\ell \frac{(2\ell+1)}{4\pi} C_\ell^{TT} W_\ell^2 & (\text{A2}) \\ \langle \delta_T \xi_{\phi\phi} \rangle &= \langle \delta_T \xi_{\theta\theta} \rangle = - \sum_\ell \frac{(2\ell+1)}{4\pi} \frac{\ell(\ell+1)}{2} C_\ell^{TT} W_\ell^2 \\ \langle \xi_{\theta\theta}^2 \rangle &= \sum_\ell \frac{(2\ell+1)}{4\pi} \frac{(3\ell(\ell+1) - 2)\ell(\ell+1)}{8} C_\ell^{TT} W_\ell^2 \\ \langle \xi_{\theta\theta} \xi_{\phi\phi} \rangle &= \sum_\ell \frac{(2\ell+1)}{4\pi} \frac{(\ell(\ell+1) + 2)\ell(\ell+1)}{8} C_\ell^{TT} W_\ell^2 \\ \langle \xi_{\phi\theta}^2 \rangle &= \sum_\ell \frac{(2\ell+1)}{4\pi} \frac{(\ell+2)(\ell+1)\ell(\ell-1)}{8} C_\ell^{TT} W_\ell^2 \end{aligned}$$

where $W_\ell = \exp(-\theta_{\text{beam}}^2 \ell(\ell+1)/2)$ and $\theta_{\text{beam}} \equiv \theta_{\text{FWHM}}/\sqrt{8 \ln(2)}$ for a Gaussian smoothing kernel associated with beam transfer function (Bond & Efstathiou 1987; Heavens & Sheth 1999; Hikage et al. 2006). Also C_ℓ^{TT} is the power spectrum of CMB temperature fluctuations. Other terms are $\langle \eta_\phi^2 \rangle = \langle \eta_\theta^2 \rangle = -\langle \delta_T \xi_{\phi\phi} \rangle$ and $\langle \xi_{\theta\theta}^2 \rangle = \langle \xi_{\phi\phi}^2 \rangle$.

REFERENCES

Ade P., et al., 2014a, *Astronomy & Astrophysics*, 571, A9
Ade P. A., et al., 2014b, *Astronomy & Astrophysics*, 571, A12
Ade P. A., et al., 2014c, *Astronomy & Astrophysics*, 571, A24
Ade P. A., et al., 2014d, *Astronomy & Astrophysics*, 571, A25
Ade P., et al., 2016a, *Astronomy & Astrophysics*, 594, A12
Ade P. A., et al., 2016b, *Astronomy & Astrophysics*, 594, A13
Ade P., et al., 2016c, *Astronomy & Astrophysics*, 594, A16
Adler R., 1981, *The Geometry of Random Fields*, Chichester: Wiley, 1981
Adler R., Taylor J. E., 2011, *Topological Complexity of Smooth Random Functions: École D'Été de Probabilités de Saint-Flour XXXIX-2009*. Springer Science & Business Media
Adler R. J., Bobrowski O., Borman M. S., Subag E., Weinberger S., et al., 2010, in , *Borrowing strength: theory powering applications—a Festschrift for Lawrence D. Brown*. Institute of Mathematical Statistics, pp 124–143
Aghanim N., et al., 2016, *Astron. Astrophys.*, 594, A11
Arbuzov P., Kotok E., Naselsky P., Novikov I., 1997, *International Journal of Modern Physics D*, 6, 409
Bardeen J. M., Bond J. R., Kaiser N., Szalay A. S., 1986, *Astrophys. J.*, 304, 15

covariance matrix which is represented in Eq. (2) is given by:

Barreiro R., Sanz J., Martínez-González E., Cayón L., Silk J., 1997, *The Astrophysical Journal*, 478, 1
Bennett D. P., Bouchet F. R., 1990, *Physical Review D*, 41, 2408
Bernardeau F., Colombi S., Gaztanaga E., Scoccimarro R., 2002, *Physics reports*, 367, 1
Bevis N., Hindmarsh M., Kunz M., Urrestilla J., 2008, *Phys. Rev. Lett.*, 100, 021301
Bevis N., Hindmarsh M., Kunz M., Urrestilla J., 2010, *Phys. Rev.*, D82, 065004
Bond J., Efstathiou G., 1987, *Monthly Notices of the Royal Astronomical Society*, 226, 655
Borgani S., 1995, *Physics Reports*, 251, 1
Bouchet F. R., Bennett D. P., Stebbins A., 1988, *Nature*, 335, 410
Brill P. H., 2000, *CORS Bulletin*, 34, 9
Cayón L., Smoot G., 1995, *The Astrophysical Journal*, 452, 487
Codis S., Pichon C., Pogosyan D., Bernardeau F., Matsubara T., 2013, *Monthly Notices of the Royal Astronomical Society*, 435, 531
Cole A., Shiu G., 2018, *Journal of Cosmology and Astroparticle Physics*, 2018, 025
Coles P., 1988, *Monthly Notices of the Royal Astronomical Society*, 234, 509
Colley W. N., Gott III J. R., 2015, *Monthly Notices of the Royal Astronomical Society*, 447, 2034
Colley W. N., Richard Gott III J., 2003, *Monthly Notices of the Royal Astronomical Society*, 344, 686
Cooray A., Sheth R., 2002, *Physics Reports*, 372, 1
Copeland E. J., Kibble T. W. B., 2010, *Proc. Roy. Soc. Lond.*, A466, 623
Copeland E. J., Liddle A. R., Lyth D. H., Stewart E. D., Wands D., 1994, *Phys. Rev.*, D49, 6410
Copeland E. J., Myers R. C., Polchinski J., 2004, *JHEP*, 06, 013
Davis M., Peebles P., 1983, *The Astrophysical Journal*, 267, 465
DePies M. R., Hogan C. J., 2007, *Physical Review D*, 75, 125006
Desjacques V., Crocce M., Scoccimarro R., Sheth R. K., 2010, *Physical Review D*, 82, 103529
Desjacques V., Jeong D., Schmidt F., 2018, *Physics reports*, 733, 1
Dickinson C., 2016, arXiv preprint arXiv:1606.03606
Dodelson S., 2003, *Modern cosmology*. Academic press
Doré O., Colombi S., Bouchet F. R., 2003, *Monthly Notices of the Royal Astronomical Society*, 344, 905
Doroshkevich A., 1970, *Astrophysics*, 6, 320
Dvali G., Vilenkin A., 2004, *JCAP*, 0403, 010
Fabri R., Torres S., 1996, *Astronomy and Astrophysics*, 307, 703
Fang W., Li B., Zhao G.-B., 2017, *Physical review letters*, 118, 181301
Fraisse A. A., Ringeval C., Spergel D. N., Bouchet F. R., 2008, *Physical Review D*, 78, 043535
Futamase T., Takada M., 2000, arXiv preprint astro-ph/0009153
Gay C., Pichon C., Pogosyan D., 2012, *Physical Review D*, 85,

- 023011
- Ghasemi Nezhadhighi M., Movahed S., Yasseri T., Vaez Allaei S. M., 2017, *Journal of Applied Physics*, 122, 085302
- Ghasemi F., Bahraminasab A., Movahed M. S., Rahvar S., Sreenivasan K., Tabar M. R. R., 2006, *Journal of Statistical Mechanics: Theory and Experiment*, 2006, P11008
- Gorski K. M., Hivon E., Banday A., Wandelt B. D., Hansen F. K., Reinecke M., Bartelmann M., 2005, *The Astrophysical Journal*, 622, 759
- Gott III J. R., Melott A. L., Dickinson M., 1986, *The Astrophysical Journal*, 306, 341
- Gott III J. R., Park C., Juszkiewicz R., Bies W. E., Bennett D. P., Bouchet F. R., Stebbins A., 1990, *The Astrophysical Journal*, 352, 1
- Gott III J. R., Colley W. N., Park C.-G., Park C., Mugnolo C., 2007, *Mon. Not. Roy. Astron. Soc.*, 377, 1668
- Hamilton A., 1993, *The Astrophysical Journal*, 417, 19
- Hamilton A., Gott III J. R., Weinberg D., 1986, *The Astrophysical Journal*, 309, 1
- Heavens A. F., Gupta S., 2001, *Monthly Notices of the Royal Astronomical Society*, 324, 960
- Heavens A. F., Sheth R. K., 1999, *Monthly Notices of the Royal Astronomical Society*, 310, 1062
- Henry Tye S. H., 2008, *Lect. Notes Phys.*, 737, 949
- Hernández-Monteagudo C., Kashlinsky A., Atrio-Barandela F., 2004, *Astronomy & Astrophysics*, 413, 833
- Hewett P. C., 1982, *Monthly Notices of the Royal Astronomical Society*, 201, 867
- Hikage C., Komatsu E., Matsubara T., 2006, *The Astrophysical Journal*, 653, 11
- Hindmarsh M. B., Kibble T. W. B., 1995, *Rept. Prog. Phys.*, 58, 477
- Hou Z., Banday A., Górski K., 2009, *Monthly Notices of the Royal Astronomical Society*, 396, 1273
- Jensen L. G., Szalay A., 1986, *The Astrophysical Journal*, 305, L5
- Kaiser N., 1984, *The Astrophysical Journal*, 284, L9
- Kashlinsky A., 2005, *Physics Reports*, 409, 361
- Kashlinsky A., Hernández-Monteagudo C., Atrio-Barandela F., 2001, *The Astrophysical Journal Letters*, 557, L1
- Kerscher M., Szapudi I., Szalay A. S., 2000, *The Astrophysical Journal Letters*, 535, L13
- Kibble T. W. B., 1976, *J. Phys.*, A9, 1387
- Kibble T. W. B., 1980, *Phys. Rept.*, 67, 183
- Kibble T. W., 2004, arXiv preprint astro-ph/0410073
- Kogut A. J., Banday A. J., Bennett C. L., Hinshaw G. F., Lubin P. M., Smoot G. F., 1995, *Astrophysical Journal*, 439, 29
- Kogut A., Banday A. J., Bennett C. L., Górski K. M., Hinshaw G., Smoot G. F., Wright E. L., 1996, *The Astrophysical Journal Letters*, 464, L29
- Komatsu E., 2002, arXiv preprint astro-ph/0206039
- Landy S. D., Szalay A. S., 1993a, *The Astrophysical Journal*, 412, 64
- Landy S. D., Szalay A. S., 1993b, *Astrophys. J.*, 412, 64
- Larson D. L., Wandelt B. D., 2004, *The Astrophysical Journal Letters*, 613, L85
- Larson D. L., Wandelt B. D., 2005, arXiv preprint astro-ph/0505046
- Lesgourges J., 2013, in , *Searching for New Physics at Small and Large Scales: TASI 2012*. World Scientific, pp 29–97
- Lesgourges J., Mangano G., Miele G., Pastor S., 2013, *Neutrino cosmology*. Cambridge University Press
- Lew B., Roukema B., 2008, *Astronomy & Astrophysics*, 482, 747
- Lewis A., Challinor A., 2006, *Physics Reports*, 429, 1
- Lewis A., Munshi D., Planck Collaboration e. a., et al., 2016, *Astronomy & Astrophysics*, 594
- Ling C., Wang Q., Li R., Li B., Wang J., Gao L., 2015, *Physical Review D*, 92, 064024
- Lumsden S., Heavens A., Peacock J., 1989, *Monthly Notices of the Royal Astronomical Society*, 238, 293
- Majumdar M., Christine-Davis A., 2002, *JHEP*, 03, 056
- Malik K. A., Wands D., 2009, *Phys. Rept.*, 475, 1
- Martinez V. J., Saar E., 2001, *Statistics of the galaxy distribution*. CRC press
- Matsubara T., 1994, *The Astrophysical Journal*, 434, L43
- Matsubara T., 1996, *The Astrophysical Journal*, 457, 13
- Matsubara T., 2003, *The Astrophysical Journal*, 584, 1
- Matsubara T., 2010, *Physical Review D*, 81, 083505
- Matsubara T., 2020, arXiv preprint arXiv:2001.05702
- Matsubara T., Yokoyama J., 1996, *The Astrophysical Journal*, 463, 409
- Mecke K., Bucheri T., Wagner H., 1994, *Astron. Astrophys.*, 288, 697
- Movahed M. S., Khosravi S., 2011, *Journal of Cosmology and Astroparticle Physics*, 2011, 012
- Movahed M. S., Ghasemi F., Rahvar S., Tabar M. R. R., 2011, *Physical Review E*, 84, 021103
- Movahed M. S., Javanmardi B., Sheth R. K., 2013, *Monthly Notices of the Royal Astronomical Society*, 434, 3597
- Novaes C., Bernui A., Marques G., Ferreira I., 2016, *Monthly Notices of the Royal Astronomical Society*, 461, 1363
- Peacock J., Heavens A. F., 1985, *Monthly Notices of the Royal Astronomical Society*, 217, 805
- Peebles P. J. E., 1980, *The large-scale structure of the universe*. Princeton university press
- Pogosian L., Tye S.-H. H., Wasserman I., Wyman M., 2003, *Physical Review D*, 68, 023506
- Pogosyan D., Pichon C., Gay C., Prunet S., Cardoso J., Sousbie T., Colombi S., 2009, *Monthly Notices of the Royal Astronomical Society*, 396, 635
- Pogosyan D., Pichon C., Gay C., 2011, *Physical Review D*, 84, 083510
- Polchinski J., 2005, *Int. J. Mod. Phys.*, A20, 3413
- Politzer H. D., Wise M. B., 1984, *The Astrophysical Journal*, 285, L1
- Pranav P., et al., 2019, *Monthly Notices of the Royal Astronomical Society*, 485, 4167
- Reischke R., Maturi M., Bartelmann M., 2015, *Monthly Notices of the Royal Astronomical Society*, 456, 641
- Renaux-Petel S., 2015, *Comptes Rendus Physique*, 16, 969
- Rice S. O., 1944, *Bell Labs Technical Journal*, 23, 282
- Rice S. O., 1945, *The Bell System Technical Journal*, 24, 46
- Rice S., 1954, ed. N. Wax, Dover Publ. Inc.(NY)
- Ringeval C., Bouchet F. R., 2012, *Physical Review D*, 86, 023513
- Ringeval C., Sakellariadou M., Bouchet F. R., 2007, *Journal of Cosmology and Astroparticle Physics*, 2007, 023
- Rossi G., 2013, *Monthly Notices of the Royal Astronomical Society*, 430, 1486
- Rossi G., Sheth R. K., Park C., Hernández-Monteagudo C., 2009, *Monthly Notices of the Royal Astronomical Society*, 399, 304
- Rossi G., Chingangbam P., Park C., 2011, *Monthly Notices of the Royal Astronomical Society*, 411, 1880
- Ryden B. S., 1988, *The Astrophysical Journal*, 333, L41
- Ryden B. S., Melott A. L., Craig D. A., Gott III J. R., Weinberg D. H., Scherrer R. J., Bhavsar S. P., Miller J. M., 1989, *The Astrophysical Journal*, 340, 647
- Sakellariadou M., 1997, *Int. J. Theor. Phys.*, 36, 2503
- Sakellariadou M., 2007, *Lect. Notes Phys.*, 718, 247
- Sarangi S., Tye S. H. H., 2002, *Phys. Lett.*, B536, 185
- Sazhin M., 1985, *Monthly Notices of the Royal Astronomical Society*, 216, 25P
- Schmalzing J., Górski K. M., 1998, *Monthly Notices of the Royal Astronomical Society*, 297, 355
- Schmalzing J., Buchert T., Kerscher M., 1995, *Proc. Int. Sch. Phys. Fermi*, 132, 281
- Shahbazi F., Sobhanian S., Tabar M. R. R., Khorram S., Frootan

- G., Zahed H., 2003, *Journal of Physics A: Mathematical and General*, 36, 2517
- Shellard E. P. S., 1987, *Nucl. Phys.*, B283, 624
- Szalay A. S., 1988a, in *Symposium-International Astronomical Union*. pp 163–167
- Szalay A. S., 1988b, in *Large Scale Structures of the Universe*. p. 163
- Szalay A. S., 1988c, *The Astrophysical Journal*, 333, 21
- Szapudi I., Szalay A. S., 1998, *The Astrophysical Journal Letters*, 494, L41
- Takada M., Futamase T., 2001, *The Astrophysical Journal*, 546, 620
- Takada M., Komatsu E., Futamase T., 2000, *The Astrophysical Journal Letters*, 533, L83
- Taqqu M. S., 1977, *Probability Theory and Related Fields*, 40, 203
- Tojeiro R., Castro P., Heavens A., Gupta S., 2006, *Monthly Notices of the Royal Astronomical Society*, 365, 265
- Vachaspati T., Vilenkin A., 1984, *Physical Review D*, 30, 2036
- Vafaei Sadr A., Movahed S., Farhang M., Ringeval C., Bouchet F., 2017, *Monthly Notices of the Royal Astronomical Society*, 475, 1010
- Vafaei Sadr A., Farhang M., Movahed S., Bassett B., Kunz M., 2018, *Monthly Notices of the Royal Astronomical Society*, 478, 1132
- Vilenkin A., 1981, *Phys. Rev. Lett.*, 46, 1169
- Vilenkin A., 1985, *Phys. Rept.*, 121, 263
- Vilenkin A., Shellard E. P. S., 2000, *Cosmic strings and other topological defects*. Cambridge University Press
- Vittorio N., Juskiewicz R., 1987, *The Astrophysical Journal*, 314, L29
- Zeldovich Ya. B., 1980, *Mon. Not. Roy. Astron. Soc.*, 192, 663
- über Inhalt H. H. V., 1957, *Oberfläche und Isoperimetrie*

This paper has been typeset from a $\text{\TeX}/\text{\LaTeX}$ file prepared by the author.